Research Article

Hanpeng Deng, Hunan Jiang, Kun Wang, Zhenyu Wang, Bin Wang, Zuowan Zhou, and Jinyang Li*

Coupling the vanadium-induced amorphous/crystalline $NiFe_2O_4$ with phosphide heterojunction toward active oxygen evolution reaction catalysts

https://doi.org/10.1515/ntrev-2022-0450
received April 25, 2022; accepted May 15, 2022

Abstract: Developing efficient and robust electrocatalysts is increasingly essential for water splitting, severely hindered by the sluggish four-electron transfer process of oxygen evolution reaction (OER). Amorphous/crystalline heterophase engineering has recently emerged as a promising electronic modulation approach for OER catalysts but suffers from poor conductivity of the amorphous structure. Here, we coupled the amorphous/crystalline $NiFe_2O_4$ induced by vanadium doping with NiP heterojunction, highlighting the synergistic effect in modulating the electronic structures and the complementary effect in promoting conductivity. As a superior electrocatalyst to commercial RuO_2, the as-prepared NFO-$V_{0.3}$-P showed a low overpotential of 277 mV at the current density of 20 mA cm^{-2}, a Tafel slope of 45 mV dec^{-1}, and long-term stability. The excellent OER catalytic activity is attributed to the synergistic effect at the heterophase interface with rich active sites, fine-tuning of electronic regulation, and enhanced conductivity.

Keywords: spinel oxide, OER, electrocatalyst, doping, heterojunction, heterophase

1 Introduction

Electrolysis of water to produce hydrogen and oxygen is a promising approach to solving current energy crisis and environmental pollution problems [1–3]. The bottleneck of electrochemical water splitting is the slow oxygen evolution reaction (OER) on the anode [4], while the commonly used noble metal iridium (Ir)-based and ruthenium (Ru)-based catalysts are limited by their high cost and poor stability [5–7]. Therefore, the development of earth-abundant transition metals as high-performance OER electrocatalysts has attracted more and more researchers' attention [8–10]. For example, spinel nickel ferrite $NiFe_2O_4$ has become a promising catalyst due to its advantages such as low cost, easy preparation, and easy structure control [11]. Researchers have prepared a series of $NiFe_2O_4$ catalysts with different structures and properties by hydrothermal method [12], solvothermal method [13], and sol–gel method [14]. However, pure $NiFe_2O_4$ is not suitable for OER due to the shortcomings of active sites and electronic structure and needs to be modified [15]. There are two main strategies to prepare transition metals into high-performance OER catalysts. The first is to adjust the morphology, geometry, and size of materials to increase the number of active centers [16–18]. The second is to improve the intrinsic activity

* **Corresponding author: Jinyang Li,** Key Laboratory of Advanced Technologies of Materials (Ministry of Education), School of Materials Science and Engineering, Southwest Jiaotong University, Chengdu, 610031, China; Yibin Institute of Southwest Jiaotong University, Yibin, 644000, China, e-mail: jinyang.li@swjtu.edu.cn
Hanpeng Deng, Hunan Jiang, Kun Wang, Zhenyu Wang: Key Laboratory of Advanced Technologies of Materials (Ministry of Education), School of Materials Science and Engineering, Southwest Jiaotong University, Chengdu, 610031, China
Bin Wang: Key Laboratory of Advanced Technologies of Materials (Ministry of Education), School of Materials Science and Engineering, Southwest Jiaotong University, Chengdu, 610031, China; Yibin Institute of Southwest Jiaotong University, Yibin, 644000, China
Zuowan Zhou: Key Laboratory of Advanced Technologies of Materials (Ministry of Education), School of Materials Science and Engineering, Southwest Jiaotong University, Chengdu, 610031, China; Yibin Institute of Southwest Jiaotong University, Yibin, 644000, China; Institute of Frontier Science and Technology, Southwest Jiaotong University, Chengdu 610031, China

of each active center by adjusting the crystal and electronic structures [19–21].

Doping can lead to heterophase, exhibiting optimized catalytic activity [22,23]. Recently, it has been reported that doping can induce the formation of amorphous/crystalline heterophase, resulting in abundant surface defects and coordinatively unsaturated sites, thereby increasing the exposure of active sites [24]. Han *et al.* fabricated F-doped Co_2B with a high-density crystalline/amorphous interface that significantly enhances OER activity [25]. V is favored among all the dopants due to its low cost and robust existence in various valence states [26]. Li *et al.* reported that V promoted the transfer of electrons from Ni to VO_x and reduced the adsorption energy; VO_x also led to significant decay of the Ni lattice, resulting in amorphous/crystalline heterophase with increased electrochemically active surface area [27]. However, the low electrical conductivity of the amorphous structure severely limits the charge transfer during catalysis [28]. The built-in electric field at the heterojunction interface promotes charge transfer and redistribution, effectively regulating the electronic structure and enhancing conductivity [29]. Thus, heterojunction might be a remedy for the amorphous/crystalline structure. Furthermore, although spinel oxides have been intensively reported previously, the amorphous/crystalline heterophase spinel oxides coupled with phosphide heterojunction have not been reported yet. Therefore, it is desirable to construct such a hybrid interface and investigate the synergistic electronic regulation effect for boosting OER.

Based on the above challenges, we combined V-doping and phosphide heterojunction strategies to construct an amorphous/crystalline heterophase catalyst NFO-$V_{0.3}$-P to synergistically optimize the electrical structure and conductivity for OER. The introduction of V weakened the crystallization ability of spinel $NiFe_2O_4$ and induced the formation of amorphous/crystalline heterophase with abundant oxygen vacancies and uncoordinated sites. Although V doping alone promoted the rearrangement of the electronic structure, the addition of NiP heterostructure improved the amorphous phase's poor conductivity and further optimized the electronic structure by reducing the e_g occupancy of Ni to be around 1.2. The as-prepared NFO-$V_{0.3}$-P achieved a low overpotential of 277 mV at the current density of 20 mA cm^{-2}, a Tafel slope of 45 mV dec^{-1}, and long-term stability in alkaline media. This work provides an insightful coupling strategy for designing advanced OER electrocatalysts and performs a practical evaluation from the perspective of the e_g occupancy in revealing its potential in synergistic electronic regulation.

2 Experimental

2.1 Materials

Nickel nitrate hexahydrate ($Ni(NO_3)_2{\cdot}6H_2O$, analytically pure), iron(III) nitrate nonahydrate ($Fe(NO_3)_3{\cdot}9H_2O$, analytically pure), hexadecyl trimethyl ammonium bromide (CTAB, >98%), vanadium(III) chloride (VCl_3, >97%), ammonia ($NH_3{\cdot}H_2O$, analytically pure), sodium hypophosphite (NaH_2PO_2, analytically pure), potassium hydroxide (KOH, analytically pure) were purchased from Kelong Chemical Agent. Ruthenium oxide (RuO_2, 99.95%) was purchased from Alfa Aeser. Nafion solution (5%) was purchased from Dupont. All chemicals were used as received without further purification.

2.2 Synthesis of NFO electrocatalyst

First, $Ni(NO_3)_2{\cdot}6H_2O$ (1 mmol), $Fe(NO_3)_3{\cdot}9H_2O$ (2 – x mmol), and CTAB (0.2 g) were dissolved in a mixed solution of 20 mL deionized water and 10 mL ethanol and stirred for 1 h to obtain a homogeneous solution. Then, $NH_3{\cdot}H_2O$ (3 mL) was added dropwise under vigorous stirring. Subsequently, the solution was transferred to a 50 mL Teflon-lined autoclave and heated at 180°C for 12 h. The precipitate was collected by centrifugation, washed with ethanol and water, and dried at 50°C overnight. Finally, the precursor was ground and calcined in a muffle furnace at 400°C for 4 h to obtain the NFO catalyst.

2.3 Synthesis of NFO-V_x electrocatalysts

Except for the raw materials, the preparation method of NFO-V_x (x = 0.1, 0.3, 0.5) catalysts is the same as that of NFO. First, $Ni(NO_3)_2{\cdot}6H_2O$ (1 mmol), $Fe(NO_3)_3{\cdot}9H_2O$ (2 – x mmol), VCl_3 (x mmol), and CTAB (0.2 g) were dissolved in a mixed solution of 20 mL deionized water and 10 mL ethanol and stirred for 1 h to obtain a homogeneous solution. The following preparation steps are exactly the same as that of NFO catalyst, and finally, the NFO-V_x (x = 0.1, 0.3, 0.5) catalysts were obtained.

2.4 Synthesis of NFO-V_x-P electrocatalyst

The prepared NFO-$V_{0.3}$ and NaH_2PO_2 were loaded in two porcelain boats with a mass ratio of 1:3 and were placed

downstream and upstream of the tube furnace, respectively. The NFO-$V_{0.3}$-P catalyst was prepared by heating to 300°C at a heating rate of 2°C min^{-1} under an Ar atmosphere for 2 h.

2.5 Material characterizations

The phase structure of the catalysts was determined using an X'pert Pro powder X-ray diffraction (XRD) from 20° to 80°. Scanning electron microscopy (SEM) images and elemental mapping were obtained using a JEOL JSM-7800 F field-emission SEM. Transmission electron microscope (TEM) images were taken using a Tecnai G220 (S-TWIN, FEI). X-ray photoelectron spectroscopy (XPS) was measured by Thermo ESCALAB 250XI. Electron paramagnetic resonance (EPR) spectra were obtained using a Bruker EMX plus X-band EPR spectrometer.

2.6 Electrochemical measurements

Electrochemical measurements were performed on Ivium Vertex. C electrochemical workstation in a three-electrode electrochemical cell. Pt sheet and Hg/HgO were used as the counter electrode and reference electrode. 1 M KOH solution was used as the electrolyte; 5 mg of catalyst was ultrasonically dispersed in a mixed solution of ethanol (900 µL) and Nafion (5 wt%, 100 µL) to obtain a homogeneous catalyst ink. Then, 100 µL of the as-prepared ink was drop cast onto nickel foam (1 cm × 1 cm) to prepare the working electrode with a catalyst loading of 0.5 mg cm^{-2}.

The electrolyte was bubbled with O_2 for 30 min before the OER measurements and maintained an O_2-saturated electrolyte throughout the measurement. Cyclic voltammetry (CV) between 0 and 1 V *vs* Hg/HgO at a scan rate of 50 mV s^{-1} was performed to activate the catalysts surface until a steady-state CV curve was established. Linear sweep voltammetry (LSV) curves were collected at a scan rate of 5 mV s^{-1} and corrected by solution resistance (R_s). Electrochemical impedance spectroscopy (EIS) was performed at open circuit potential over the frequency range between 100 kHz and 0.1 Hz. By calibrating the reference electrode (Figure S1), all potential values were calibrated concerning the reversible hydrogen electrode (RHE) by $E_{RHE} = E_{Hg/HgO} + 0.93$ V. Overpotentials (η) was calculated based on the formula $\eta = E_{RHE} - 1.23$ V. Electrochemical active surface areas (ECSA) were obtained by measuring electrochemical double-layer capacitance (C_{dl}) of catalysts. Chronopotentiometry measurements evaluated stability at the current density of 20 and 100 mA cm^{-2}.

3 Results and discussion

3.1 Characterization analysis of catalysts

The synthesis of the NFO-$V_{0.3}$-P catalyst involved two steps. As shown in Figure 1, the first step was to dope V into the catalyst by hydrothermal method. CTAB as a

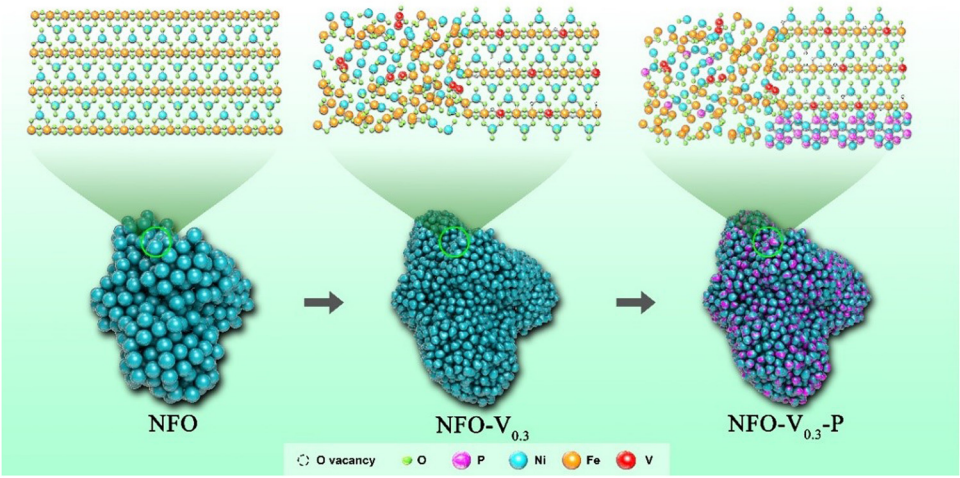

Figure 1: Catalyst preparation process diagram.

surfactant modulated the shape and size of nanoparticles and prevented excessive aggregation of nanoparticles. After the first heat treatment, transition metal oxide nanoparticles with the structural formula of $NiV_{0.3}Fe_{1.7}O_4$ were prepared and denoted as NFO-$V_{0.3}$. In the second step, a small amount of NaH_2PO_2 was pyrolyzed in a tube furnace to grow metal phosphide on the catalyst surface to obtain the final catalyst, which was named NFO-$V_{0.3}$-P. V and P have been successfully introduced into the catalyst system in the corresponding steps, as shown in Figure 2(a) and Figures S2, S3. The distribution of each element in the catalyst is uniform.

The catalysts' morphology and crystal structure evolution after V introduction and surface partial phosphating were characterized using XRD and TEM. As shown in Figure 2(b) and Figure S4, the diffraction angles and diffraction intensity of the NFO catalyst are consistent with those of $NiFe_2O_4$ (PDF #10-0325), indicating the successful preparation of an inverse spinel transition metal oxide with the good crystal structure. The catalyst after

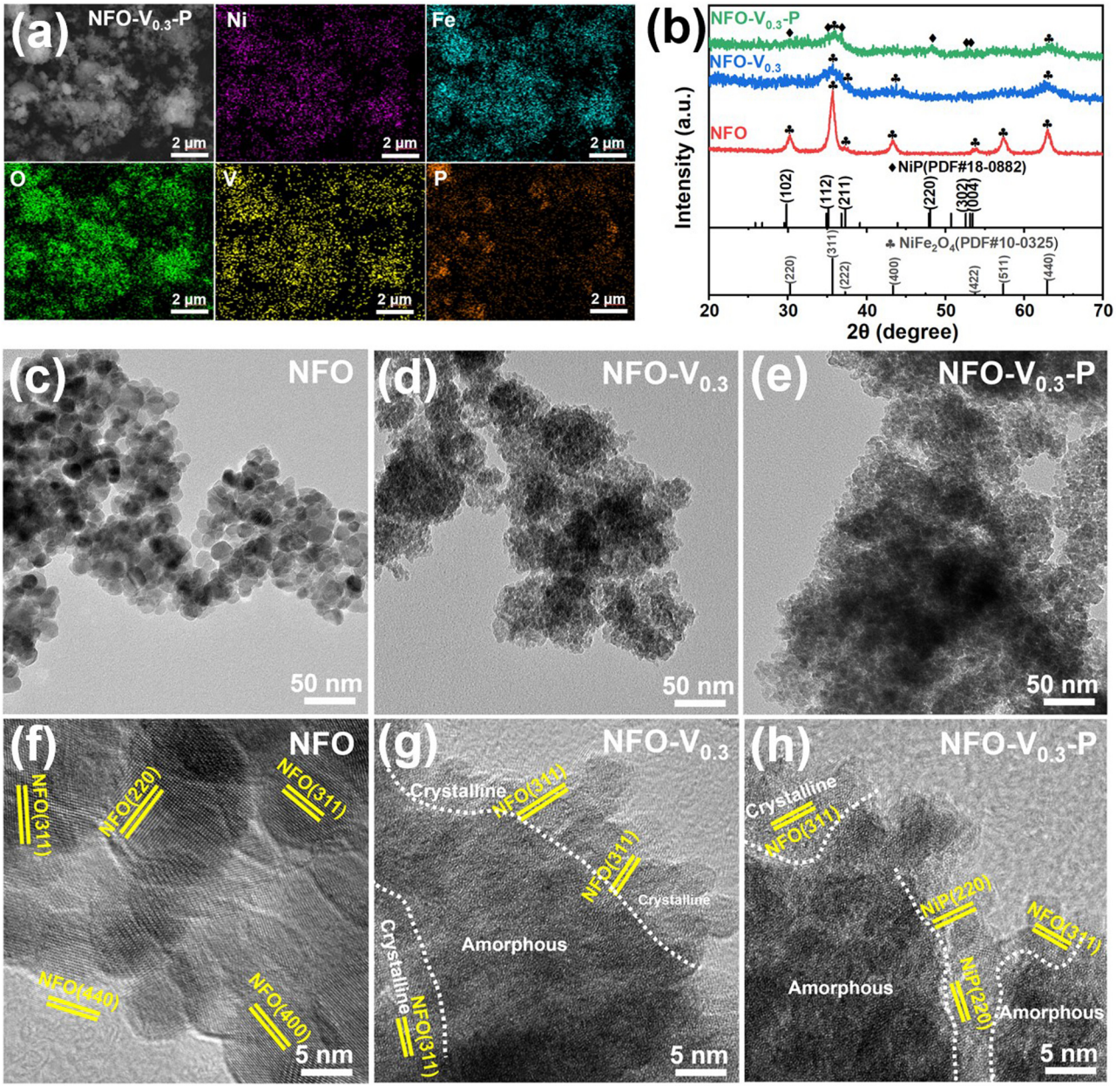

Figure 2: (a) SEM image and the corresponding elemental mapping of NFO-$V_{0.3}$-P. (b) XRD patterns of NFO, NFO-$V_{0.3}$, NFO-$V_{0.3}$-P. (c–e) TEM and (f–h) HRTEM image of NFO, NFO-$V_{0.3}$, NFO-$V_{0.3}$-P.

V doping also shows a similar XRD pattern, but the diffraction intensity is reduced, indicating that the crystalline nature was affected due to the V doping. With the increase in V content, the diffraction intensity gradually decreases, indicating that the weakening of crystallinity is caused by V and is closely related to the content of V. The crystallinity of the catalysts is NFO (93.9%), NFO-$V_{0.1}$ (91.6%), NFO-$V_{0.3}$ (59.2%), and NFO-$V_{0.5}$ (49.3%), respectively. The XRD pattern of NFO-$V_{0.3}$-P shows that the partial phosphating of the surface does not significantly change the original crystal structure of the catalyst. The new diffraction peaks with low intensity at 35.15°, 39.15°, and 48.07° correspond to (112), (211), and (220) crystal planes of NiP, respectively, which indicate that NiP appeared after phosphating.

TEM and HRTEM images provide more details on the changes in the catalyst structure. Figure 2(c) shows the polycrystalline structure of NFO, consisting of irregular nanoparticles with a particle size of 10 nm. The lattice fringes corresponding to $NiFe_2O_4$ on the (220), (311), (440), and (400) planes are observed in Figure 2(f), which verifies the above-mentioned XRD characterization. As shown in the TEM image of NFO-$V_{0.3}$ (Figure 2d), the polycrystalline structure still exists, but the nanoparticle size is significantly reduced. The corresponding HRTEM (Figure 2g) shows a sizeable blurred area without visible lattice fringes, recognized as the amorphous phase, which shows that the introduction of V in the catalyst weakens the crystallization ability of NFO-$V_{0.3}$. The introduction of a small amount of V causes part of Fe to be replaced by V. Due to the differences in atomic radius and electronic structure of V and Fe, the presence of V in the crystal lattice hinders the crystallization process, thereby weakening the crystallization ability of the catalyst [24]. Thus, part of the crystalline phase is transformed into an amorphous phase. At the same time, the limited crystallization ability prevents the catalyst nanoparticles from growing large enough, resulting in the phenomenon of nanoparticle size reduction after V doping. With an appropriate amount of V doping, some regions in the catalyst are transformed into the amorphous phase, but the rest can still be crystallized normally. The amorphous/crystalline mixed heterophase is constructed by adjusting the amount of V doping. The amorphous/crystalline mixed heterophase structure in NFO-$V_{0.3}$ provides many vacancies and interfacial defects, providing more reactive sites for catalytic reactions [30]. As shown in Figure 2(h), such an amorphous/crystalline heterophase structure is preserved after phosphating in NFO-$V_{0.3}$-P. The lattice diffraction fringes correspond to the NiP (122) plane to support the XRD characterization.

XPS was used to further evaluate the surface chemical composition and valence state of the catalysts. As shown in Figure S6(a), the existence of the V 2p peak and P 2p peak can be observed in the XPS total spectra of the three catalysts, verifying the existence of V and P elements. On the high-resolution P 2p XPS spectrum of NFO-$V_{0.3}$-P (Figure S6b), the doublet peak in the 127–131 eV region is ascribed to P-metal bonding [31]. The broad peak centered at 132.8 eV comes from the P–O bonding of phosphorus species exposed to air [32], which further proves the existence of metal phosphide on the catalyst surface.

For transition metal oxides, the e_g occupancy of the transition metal ions at the active site is an essential descriptor of OER activity because the e_g orbitals directly participate in σ bonding with surface oxygen [33]. A small e_g occupancy will lead to strong oxygen binding force, and the intermediate cannot be effectively desorbed; a large e_g occupancy will inhibit the activation of oxygen and weaken the binding force of the intermediate [34]. Previous studies have found that when the e_g occupancy is around 1.2, an ideal balance will be reached, and the catalyst shows the optimal OER activity [35,36]. Since Ni^{2+} has a valence electron configuration of ($t_{2g}6$ e_g2), it can be assumed that Ni^{2+} ($e_g = 2$) is in a high-spin state and Ni^{3+} ($e_g = 1$) is in a high-spin state. According to the ratio of Ni^{2+} and Ni^{3+}, the e_g occupy can be calculated [37]. As shown in Figure 3(a), with the introduction of *V*, a high oxidation state peak corresponding to Ni^{3+} appears at 856.28 eV, and the characteristic peak corresponding to Ni^{2+} is significantly reduced. According to the characteristic peak area $Ni^{3+}/Ni^{2+} = 1.23$, the calculated e_g occupancy is approximately 1.44. It is also observed in Figure 3(b) that the V $2p_{3/2}$ peak, which should be observed at 517.5 eV, appears at 517 eV. The lower valence is due to the acceptance of electrons from Ni. After growing the phosphide heterojunction, the corresponding binding energy of Ni $2p_{3/2}$ shifts positively from 855.08 to 855.38 eV, and the binding energy of the V $2p_{3/2}$ peak (Figure S3d) further decreases to 516.8 eV. The ratio of Ni^{3+}/Ni^{2+} continues to increase, and the e_g occupancy is calculated to be 1.26 by the ratio, which means the oxidation state of Ni is higher. The characteristic peak at 853.4 eV is attributed to Ni-P, which proves the existence of the NiP crystal phase on the catalyst surface [31].

In the Fe 2p spectra shown in Figure 3(c), the signal mainly consists of two peaks near 712.7 and 724.3 eV, which belong to Fe $2p_{3/2}$ and Fe $2p_{1/2}$, respectively [38]. The Fe^{3+} content in high valence state increases after V doping and decreases after phosphating, which means that the overall oxidation state of Fe increases first and then decreases. The heterojunction changes the internal

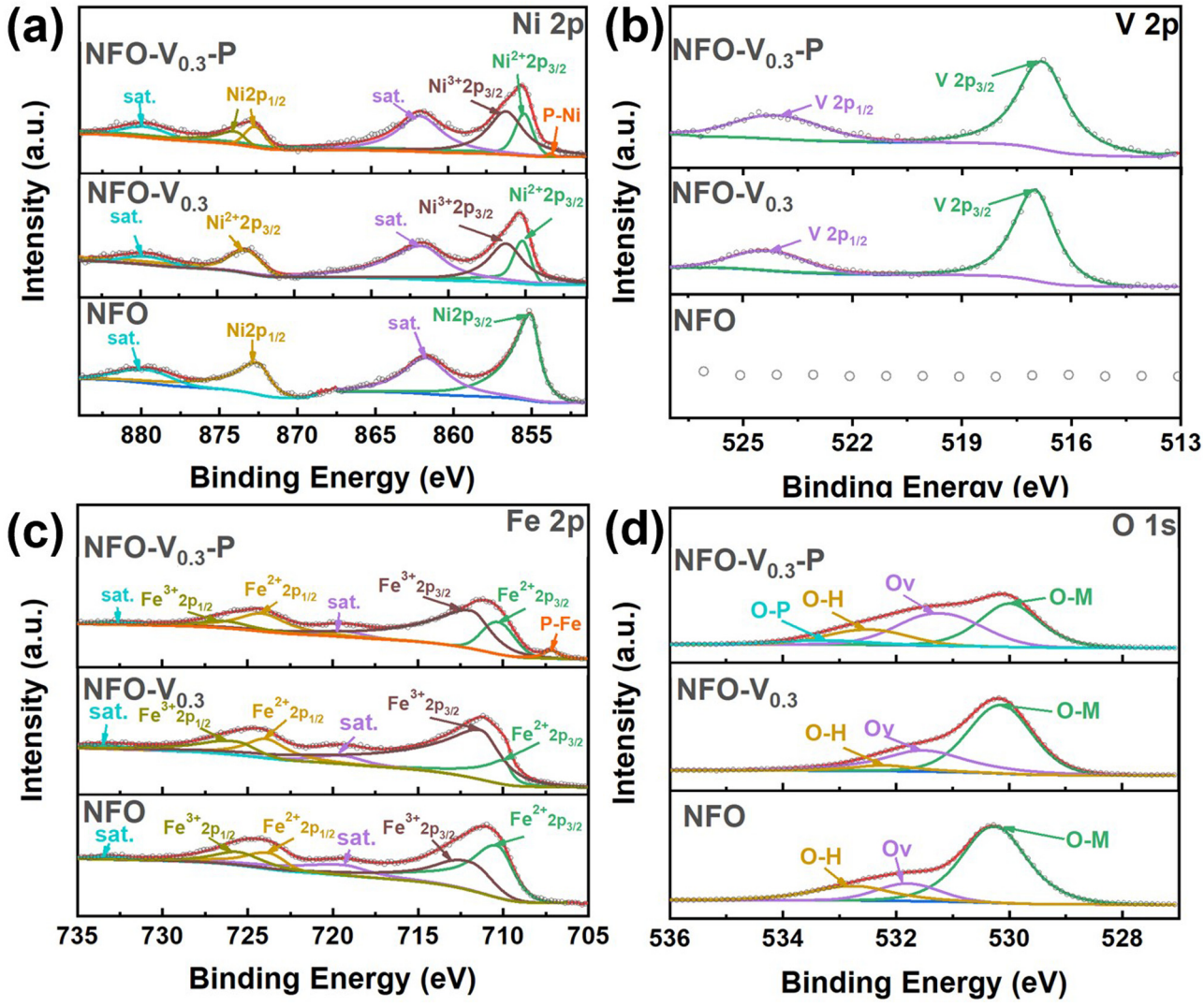

Figure 3: XPS spectra of NFO, NFO-$V_{0.3}$, NFO-$V_{0.3}$-P in (a) Ni 2p, (b) Fe 2p, (c) O 1 s, and (d) V 2p region.

electronic structure of the catalyst, and more electrons are transferred around Fe^{3+} to ensure the high oxidation state and low e_g occupancy of Ni in the catalytic active site. On the high-resolution O 1s XPS spectrum (Figure 3d), the peak at 529.7 eV is attributed to O-metal bonding, the peak at 532.6 eV is related to the hydroxyl species of surface adsorbed water molecules, while the peak at 531.2 eV is attributed to a large number of defect sites with low oxygen coordination, namely, oxygen vacancies [39]. It is clearly observed that the peak area at 531.2 eV increases with V doping and phosphide heterojunction. It indicates that amorphous/crystalline mixed heterophase and phosphide heterojunction bring more defects to the catalyst and are more favorable for OER activity [30]. EPR spectroscopy (Figure S7) also demonstrated changes in oxygen vacancies, and the enhanced EPR signal intensity at g = 2.003 is attributed to the significant increase in oxygen vacancies [40].

3.2 OER performance of catalysts

The OER activity of the catalysts was evaluated in 1 M KOH solution using a three-electrode cell, and commercial RuO_2 was used for comparison. Clearly, catalysts with different V contents showed different degrees of OER activity improvement over NFO (Figure S8). NFO-$V_{0.3}$ exhibits the lowest overpotentials of 309 and 350 mV at current densities of 20 and 100 mA cm^{-2}. The enhanced OER activity is related to the formation of amorphous/crystalline heterophase and the regulation of electronic structure induced by V in the catalyst. After constructing the

surface heterojunction, the OER activity of NFO-$V_{0.3}$-P was further enhanced. As shown in Figure 4(a), NFO-$V_{0.3}$-P exhibits low overpotentials of 277 mV and 310 mV at current densities of 20 and 100 mA cm^{-2}, far superior to commercial RuO_2. The Tafel plots (Figure 4c) converted from LSV curves can evaluate the reaction kinetics of the catalysts. NFO-$V_{0.3}$-P shows the lowest Tafel slope of 45 mV dec^{-1} among all samples, outperforming NFO (77 mV dec^{-1}), NFO-$V_{0.3}$ (54 mV dec^{-1}), and commercial RuO_2 (62 mV dec^{-1}). This indicates that the OER reaction kinetics of the catalyst are optimized by V doping and phosphide heterojunction.

As shown in Figure S9, the intrinsic catalytic activity of the catalysts can be compared by measuring the C_{dl} in the potential range from 0.83 to 1.03 V to estimate the ECSA. NFO-$V_{0.3}$ possesses the highest C_{dl} (0.3 mF cm^{-2}), attributed to more defects in the amorphous/crystalline phases, exposing the most reactive sites. Although part of the active surface area of NFO-$V_{0.3}$-P is covered by the phosphide heterojunction, the conductivity and more oxygen vacancy defects brought by phosphating significantly increase the OER activity. The charge transport properties of the catalysts can be further explored through the EIS tests. Figure 4(d) shows that NFO-$V_{0.3}$-P has the lowest R_{ct}, verifying the enhanced overall conductivity by phosphide heterojunction. Although the amorphous phase can provide many reactive sites, the electrical conductivity of both the spinel phase and the amorphous phase is relatively poor. Therefore, the phosphide heterojunction in NFO-$V_{0.3}$-P sacrifices little reactive surface area to significantly improve the overall conductivity of the catalyst, which is helpful to further improve the electrocatalytic activity.

In our designed strategies, the enhanced OER activity of the catalyst is achieved by tuning the crystal structure and electronic structure. The amorphous phase induced by V doping in the crystal structure can provide more reactive sites, and its poor conductivity is improved by the phosphide heterojunction. The V and P heteroatoms introduced by the V-doping and NiP heterojunction strategies, respectively, jointly promote electronic rearrangement. The transfer of electrons from Ni to V or other atoms achieves a higher valence state of Ni and an e_g occupancy closer to 1.2, as well as lower binding energy of the catalyst for oxygen intermediates. The optimization of the catalyst's electronic structure benefits from the synergistic regulation of the two designed strategies. Therefore, the OER activity of the catalyst is greatly enhanced after adjusting various factors such as active sites, conductivity, and e_g occupancy. Finally, we evaluated the stability and durability of the synthesized catalysts in an alkaline electrolyte by measuring chronopotentiometry

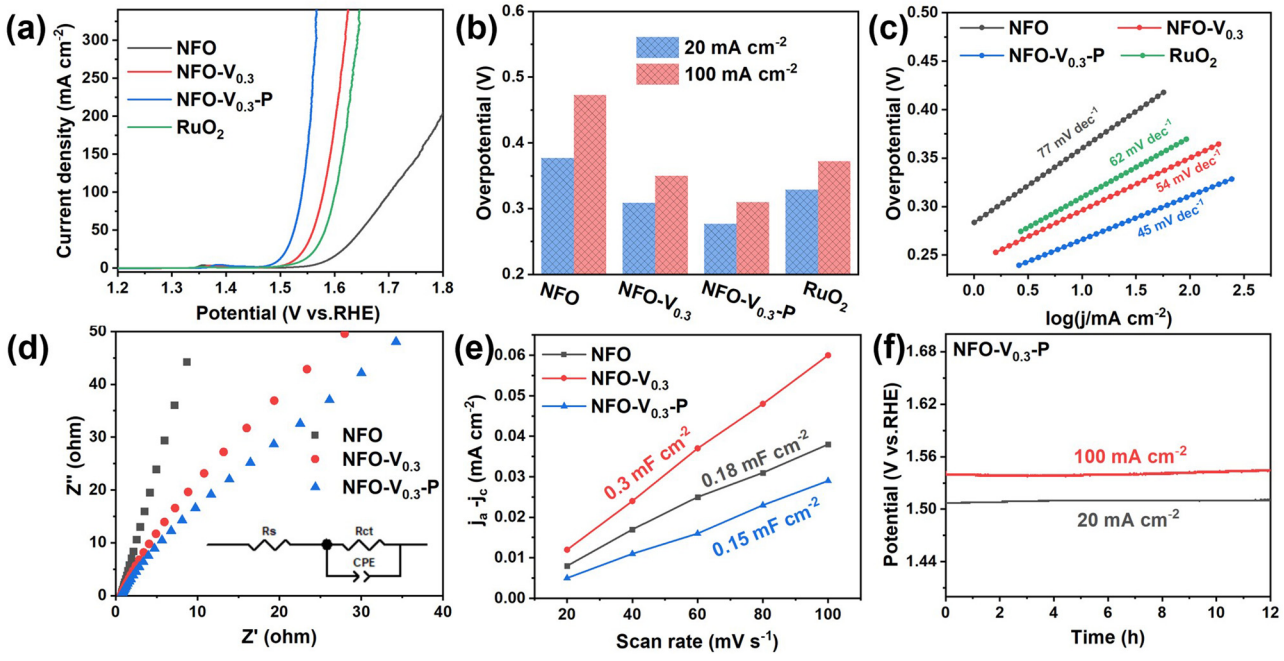

Figure 4: (a) iR-corrected LSV curves of NFO, NFO-$V_{0.3}$, NFO-$V_{0.3}$-P, and RuO_2. (b) A comparison of the overpotential values at the current densities of 20 and 100 mA cm^{-2}. (c) Corresponding Tafel plots of the polarization curves in (a). (d) Nyquist plots of NFO, NFO-$V_{0.3}$, NFO-$V_{0.3}$-P. (e) The electrochemical C_{dl} of NFO, NFO-$V_{0.3}$, and NFO-$V_{0.3}$-P. (f) OER chronopotentiometry measurement of NFO-$V_{0.3}$-P catalyst at the current densities of 20 and 100 mA cm^{-2}.

curves at 20 and 100 mA cm^{-2} in alkaline media, which is a critical factor for the large-scale application of catalysts in industrial applications. Chronopotentiometry curves of NFO-$V_{0.3}$-P in 1 M KOH (Figure 4f) show that the overpotential increased by only 4 mV after continuous electrolysis for 12 h, indicating good stability at both low and high current densities.

4 Conclusion

In conclusion, we successfully constructed amorphous/crystalline heterophase coupled with phosphide heterojunction in NFO-$V_{0.3}$-P by V doping and surface phosphating. The phosphide heterojunction improves the poor conductivity caused by the amorphous phase and achieves an e_g occupancy of 1.26 for Ni. As a result, the catalyst exhibits a low overpotential of 277 mV at 20 mA cm^{-2}, a Tafel slope of 45 mV dec^{-1}, and long-term stability in alkaline electrolytes. The amorphous/crystalline heterophase and heterojunction provide more active sites and higher conductivity and promote the electronic regulation of active sites. This work provides an instructive strategy to construct amorphous/crystalline heterophase coupled with heterojunction for synergistically enhanced OER performance.

Funding information: The work was supported by the National Natural Science Foundation of China (No. 52002338), the Science and Technology Planning Project of Sichuan Province (No. 2021ZYD0053), and Key R&D Program of Sichuan Province (2022YFSY0024).

Author contributions: All authors have accepted responsibility for the entire content of this manuscript and approved its submission.

Conflict of interest: The authors state no conflict of interest.

References

[1] Chen MP, Liu D, Zi BY, Chen YY, Liu D, Du XY, et al. Remarkable synergistic effect in cobalt-iron nitride/alloy nanosheets for robust electrochemical water splitting. J Energy Chem. 2022;65:405–14.

[2] Huang W, Peng C, Tang J, Diao FY, Yesibolati MN, Sun HY, et al. Electronic structure modulation with ultrafine Fe_3O_4 nanoparticles on 2D Ni-based metal–organic framework layers for enhanced oxygen evolution reaction. J Energy Chem. 2022;65:78–88.

[3] Rahman ST, Rhee KY, Park SJ. Nanostructured multifunctional electrocatalysts for efficient energy conversion systems: Recent perspectives. Nanotechnol Rev. 2021;10:137–57.

[4] Zhang LH, Fan Q, Li K, Zhang S, Ma XB. First-row transition metal oxide oxygen evolution electrocatalysts: Regulation strategies and mechanistic understandings. Sustain Energy Fuels. 2020;4:5417–32.

[5] Audichon T, Napporn TW, Canaff C, Morais C, Comminges C, Kokoh KB. IrO_2 coated on RuO_2 as efficient and stable electroactive nanocatalysts for electrochemical water splitting. J Phys Chem C. 2016;120:2562–73.

[6] Zagalskaya A, Alexandrov V. Mechanistic study of IrO_2 dissolution during the electrocatalytic oxygen evolution reaction. J Phys Chem Lett. 2020;11:2695–700.

[7] Audichon T, Mamaca N, Morais C, Servat K, Napporn TW, Mayousse E, et al. Synthesis of $Ru_xIr_{1-x}O_2$ anode electrocatalysts for proton exchange membrane water electrolysis. Electrocatal Appl Fuel Cell Electrol. 2013;45:47–58.

[8] Tahir M, Pan L, Zhang RR, Wang YC, Shen GQ, Aslam I, et al. High-valence-state NiO/Co_3O_4 nanoparticles on nitrogen-doped carbon for oxygen evolution at low overpotential. Acs Energy Lett. 2017;2:2177–82.

[9] Zhou YN, Fan RY, Dou SY, Dong B, Ma Y, Yu WL, et al. Tailoring electron transfer with Ce integration in ultrathin $Co(OH)_2$ nanosheets by fast microwave for oxygen evolution reaction. J Energy Chem. 2021;59:299–305.

[10] Liu Y, Ying YR, Fei LF, Liu Y, Hu QZ, Zhang GG, et al. Valence engineering via selective atomic substitution on tetrahedral sites in spinel oxide for highly enhanced oxygen evolution catalysis. J Am Chem Soc. 2019;141:8136–45.

[11] Singh NK, Singh RN. Electrocatalytic properties of spinel type $Ni_xFe_{3-x}O_4$ synthesized at low temperature for oxygen evolution in KOH solutions. Indian J Chem Sect A Inorg Bio-Inorg Phys Theor Anal Chem. 1999;38:491–5.

[12] Balasubramanian P, He SB, Jansirani A, Deng HH, Peng HP, Xia XH, et al. Engineering of oxygen vacancies regulated core-shell N-doped carbon@$NiFe_2O_4$ nanospheres: A superior bifunctional electrocatalyst for boosting the kinetics of oxygen and hydrogen evaluation reactions. Chem Eng J. 2021;405:126732.

[13] Yuan FF, Cheng XM, Wang MF, Ni YH. Controlled synthesis of tubular ferrite MFe_2O_4 (M = Fe, Co, Ni) microstructures with efficiently electrocatalytic activity for water splitting. Electrochim Acta. 2019;324:134883.

[14] Maruthapandian V, Mathankumar M, Saraswathy V, Subramanian B, Muralidharan S. Study of the oxygen evolution reaction catalytic behavior of $Co_xNi_{1-x}Fe_2O_4$ in alkaline medium. Acs Appl Mater Interfaces. 2017;9:13132–41.

[15] Chen Q, Wang R, Lu FQ, Kuang XJ, Tong YX, Lu XH. Boosting the oxygen evolution reaction activity of $NiFe_2O_4$ nanosheets by phosphate ion functionalization. Acs Omega. 2019;4:3493–9.

[16] Tian W, Li JY, Liu YF, Ali R, Guo Y, Deng LJ, et al. Atomic-scale layer-by-layer deposition of FeSiAl@ZnO@Al_2O_3 hybrid with threshold anti-corrosion and ultra-high microwave absorption properties in low-frequency bands. Nano-Micro Lett. 2021;13(1):161.

[17] Liao CG, Yang BP, Zhang N, Liu M, Chen GX, Jiang XM, et al. Constructing conductive interfaces between nickel oxide nanocrystals and polymer carbon nitride for efficient electrocatalytic oxygen evolution reaction. Adv Funct Mater. 2019;29:1904020.
[18] Huan TN, Rousse G, Zanna S, Lucas IT, Xu XZ, Menguy N, et al. A dendritic nanostructured copper oxide electrocatalyst for the oxygen evolution reaction. Angew Chem Int Ed. 2017;56:4792–6.
[19] Zhou Y, Zheng HY, Kravchenko II, Valentine J. Flat optics for image differentiation. Nat Photonics. 2020;14:316.
[20] Li X, Wang H, Cui ZM, Li YT, Xin S, Zhou JS, et al. Exceptional oxygen evolution reactivities on $CaCoO_3$ and $SrCoO_3$. Sci Adv. 2019;5(8):eaav6262.
[21] Wang HP, Wang J, Pi YC, Shao Q, Tan YM, Huang XQ. Double perovskite $LaFe_xNi_{1-x}O_3$ nanorods enable efficient oxygen evolution electrocatalysis. Angew Chem Int Ed. 2019;58:2316–20.
[22] Kong QQ, Feng W, Zhang Q, Zhang P, Sun Y, Yin YC, et al. Hybrid amorphous/crystalline FeNi(Oxy) hydroxide nanosheets for enhanced oxygen evolution. Chemcatchem. 2019;11:3004–9.
[23] Tuysuz H, Hwang YJ, Khan SB, Asiri AM, Yang PD. Mesoporous Co_3O_4 as an electrocatalyst for water oxidation. Nano Res. 2013;6:47–54.
[24] Kuang M, Zhang JM, Liu DB, Tan HT, Dinh KN, Yang L, et al. Amorphous/crystalline heterostructured cobalt-vanadium-iron (oxy)hydroxides for highly efficient oxygen evolution reaction. Adv Energy Mater. 2020;10(43):2002215.
[25] Han H, Choi H, Mhin S, Hong YR, Kim KM, Kwon J, et al. Advantageous crystalline-amorphous phase boundary for enhanced electrochemical water oxidation. Energy Environ Sci. 2019;12:2443–54.
[26] Li PS, Duan XX, Kuang Y, Li YP, Zhang GX, Liu W, et al. Tuning electronic structure of NiFe layered double hydroxides with vanadium doping toward high efficient electrocatalytic water oxidation. Adv Energy Mater. 2018;8(15):1703341.
[27] Li YB, Tan X, Hocking RK, Bo X, Ren HJ, Johannessen B, et al. Implanting Ni-O-VO_x sites into Cu-doped Ni for low-overpotential alkaline hydrogen evolution. Nat Commun. 2020;11(1):2720.
[28] Smith RDL, Prevot MS, Fagan RD, Zhang ZP, Sedach PA, Siu MKJ, et al. Photochemical route for accessing amorphous metal oxide materials for water oxidation catalysis. Science. 2013;340:60–3.
[29] Li SZ, Zang WJ, Liu XM, Pennycook SJ, Kou ZK, Yang CH, et al. Heterojunction engineering of $MoSe_2/MoS_2$ with electronic modulation towards synergetic hydrogen evolution reaction and supercapacitance performance. Chem Eng J. 2019;359:1419–26.
[30] Zhang LJ, Jang H, Liu HH, Kim MG, Yang DJ, Liu SG, et al. Sodium-Decorated Amorphous/Crystalline RuO_2 with rich oxygen vacancies: A robust pH-universal oxygen evolution electrocatalyst. Angew Chem Int Ed. 2021;60:18821–9.
[31] Li X, Huang WQ, Xia LX, Li YY, Zhang HW, Ma SF, et al. $NiFe_2O_4$/NiFeP heterostructure grown on nickel foam as an efficient electrocatalyst for water oxidation. Chemelectrochem. 2020;7:4047–54.
[32] Liu TT, Liu H, Wu XJ, Niu YL, Feng BM, Li W, et al. Molybdenum carbide/phosphide hybrid nanoparticles embedded P, N co-doped carbon nanofibers for highly efficient hydrogen production in acidic, alkaline solution and seawater. Electrochim Acta. 2018;281:710–6.
[33] Suntivich J, May KJ, Gasteiger HA, Goodenough JB, Shao-Horn Y. A perovskite oxide optimized for oxygen evolution catalysis from molecular orbital principles. Science. 2011;334:1383–5.
[34] Hardin WG, Mefford JT, Slanac DA, Patel BB, Wang XQ, Dai S, et al. Tuning the electrocatalytic activity of perovskites through active site variation and support interactions. Chem Mater. 2014;26:3368–76.
[35] Cai Z, Li LD, Zhang YW, Yang Z, Yang J, Guo YJ, et al. Amorphous nanocages of Cu-Ni-Fe hydr(oxy)oxide prepared by photocorrosion for highly efficient oxygen evolution. Angew Chem Int Ed. 2019;58:4189–94.
[36] Wei C, Feng ZX, Scherer GG, Barber J, Shao-Horn Y, Xu ZCJ. Cations in octahedral sites: A descriptor for oxygen electrocatalysis on transition-metal spinels. Adv Mater. 2017;29(23):1606800.
[37] Da YM, Zeng LR, Wang CY, Gong CR, Cui L. A simple approach to tailor OER activity of $Sr_xCo_{0.8}Fe_{0.2}O_3$ perovskite catalysts. Electrochim Acta. 2019;300:85–92.
[38] Fan K, Ji YF, Zou HY, Zhang JF, Zhu BC, Chen H, et al. Hollow iron-vanadium composite spheres: A highly efficient iron-based water oxidation electrocatalyst without the need for nickel or cobalt. Angew Chem Int Ed. 2017;56:3289–93.
[39] Xue WJ, Cheng F, Li ML, Hu WJ, Wu CP, Wang B, et al. Surpassing electrocatalytic limit of earth-abundant Fe^{4+} embedded in N-doped graphene for (photo)electrocatalytic water oxidation. J Energy Chem. 2021;54:274–81.
[40] Zhang L, Lu CJ, Ye F, Wu ZY, Wang YA, Jiang L, et al. Vacancies boosting strategy enabling enhanced oxygen evolution activity in a library of novel amorphous selenite electrocatalysts. Appl Catal B. 2021;284:119758.